Astrometric and Photometric Data Fusion for Resident Space Object Orbit, Attitude, and Shape Determination Via Multiple-Model Adaptive Estimation

Richard Linares*, John L. Crassidis†
University at Buffalo, State University of New York, Amherst, NY, 14260-4400
Moriba K. Jah‡
Air Force Research Laboratory, Kirtland AFB, New Mexico, 87117
Hakjae Kim§
University of Florida, Gainsville, FL 32611

This paper presents a new method, based on a multiple-model adaptive estimation approach, to determine the most probable shape of a spacecraft in orbit among a number of candidate shape models while simultaneously recovering the observed resident space object's inertial orientation and trajectory. Multiple-model adaptive estimation uses a parallel bank of filters to provide multiple resident space object state estimates, where each filter is purposefully dependent on a mutually unique resident space object model. Estimates on the conditional probability of each model given the available measurements are provided from the multiple-model adaptive estimation approach. Each filter employs the Unscented (or Sigma-Point) estimation approach, reducing passively-collected electro-optical data to infer the unknown state vector comprised of the resident space object inertial-to-body orientation, position and their respective temporal rates. Each hypothesized model results in a different observed optical cross-sectional area. The effect of solar radiation pressure may be recovered from accurate angles-data alone, if the collected measurements span a sufficiently long period of time so as to make the non-conservative mismodeling effects noticeable. However, for relatively short data arcs, this effect is weak and thus the temporal brightness of the resident space object can be used in concert with the angles data to exploit the fused sensitivity to both resident space object characteristics and associated trajectory, the very same ones which drive the non-conservative dynamic effects. Recovering these characteristics and trajectories with sufficient accuracy is shown in this paper, where the characteristics are inherent in unique resident space object models. The performance of this strategy is demonstrated via simulated scenarios.

I. Introduction

In recent years space situational awareness, which is concerned with collecting and maintaining knowledge of all objects orbiting the Earth, has gained much attention. The U.S. Air Force collects the necessary data for space object catalog development and maintenance through a global network of radars and optical sensors. Due to the fact that a limited number of sensors is available to track a large number of resident space objects (RSOs), the sparse data collected must be exploited to the fullest extent. Various sensors, such as radars,

*Graduate Student, Department of Mechanical & Aerospace Engineering. Email: linares2@buffalo.edu. Student Member AIAA.
†Professor, Department of Mechanical & Aerospace Engineering. Email: johnc@buffalo.edu, Associate Fellow AIAA.
‡Director, Advanced Sciences and Technology Research Institute for Astrodynamics (ASTRIA). Senior Member AIAA.
§Postdoctoral Associate, Department of Mechanical & Aerospace Engineering. Email: hjk.jaykim@gmail.com, Member AIAA.

exist for RSO state estimation, which typically includes position, velocity, and a non-conservative force parameter, B^*, analogous to a ballistic coefficient. Another piece of useful information is the estimation of the shape of an object, which requires knowledge of the attitude of the RSO.

Shape estimation is an important issue in the observation of RSOs, because the shape influences the dynamics of the object and may provide valuable information on the object's origin or intent. There exists a number of methods for estimating the shape of an object. These methods vary in the sensor type used, technique used to resolve shape, and effective ranges for proper shape resolution. Radar-based methods have been extensively used for shape estimation, which include radar cross-sectioning approaches[1] and range Doppler interferometry.[2] These techniques were first developed in the field of planetary radar astronomy to estimate the shape of natural satellites,[3] but then were later applied to the imaging of artificial Earth orbiting satellites. These methods are limited by the RSO size and distance. RSOs can be imaged in low-Earth orbits that are much larger in the dimension than the wavelength of the radar signal. To image RSOs smaller and farther than these ranges requires very powerful radar devices, making these economically unattractive.

Laser radar-based (LADAR) methods have also been used to estimate the shape of RSOs. LADAR provides a three-dimensional scan of the object, which can resolve shape geometry at ranges of 1 km, returning a cloud of points of the measured relative position of an object. DiMatteo[4] used LADAR scans to perform a least squares fit of the LADAR returns to previously assembled point cloud models to estimate the shape of an RSO. Licther[5] developed a filter approach to simultaneously estimate dynamic states, geometric shape, and mass model parameters of a satellite using multiple observations with LADAR sensors. In Ref. 5 a probabilistic map of the RSO is constructed using a sensor uncertainty model and the dynamics experienced by the RSO to estimate the shape of the same. Using well modeled dynamical relationships of the RSO provides enhancements to be implemented within a filter architecture in this shape estimate approach.[5]

Resolved images have been used to estimate the size and shape of satellites as well.[6] These methods work either directly with the pixels of the images or are used to identify features of the RSO. Features, such as corners, edges and markers, are located and tracked temporally to estimate higher level motion and the structure of the ridged body.[7] The feature-based methods rely on continuously identifying and tracking higher level traits of the RSO by using a Kalman filter to estimate feature location and motion parameters. Although these methods estimate the motion of features they do not by themselves provide a detailed estimate of the shape of the object and only give a sparse set of feature points of the object. Pixel-based methods rely on pixel-level information, and use the shading, texture and optical flow of the images to estimate the shape of an object at each time step using a monocular camera. Since these methods rely on pixel-level computations they typically involve very high-dimensional states and therefore are very computationally expensive. These methods are also very sensitive to pixel-level detail and are easily corrupted by unpredictable light intensities, reflective material and wrinkled surfaces. They require high resolution of the object to resolve meaningful shape estimates, and therefore are only effective for space-based sensors and or high resolution ground-based telescopes.

Some powerful ground-based telescopes, like the Air Force Maui Optical and Supercomputing (AMOS) site Advance Electro-Optical System (AEOS), can resolve RSOs such as Hubble Space Telescope and the International Space Station to very high detail, but most objects are too small and or too distant (making them dim) to lend themselves to ground-based resolved imaging.[8] For example operational RSOs in geosynchronous orbits and "micro" and "nano" satellites are too small to be resolved using ground-base optical observations. Angular measurements of these smaller objects are still made to provide their coordinates as they traverse the sky. Although the amount of light collected from these objects is small, information can still be extracted from these data which can be used to resolve their shapes.

Light curves (the RSO temporal brightness) have also been used to estimate the shape for an object. Light curve approaches have been studied to estimate the shape and state of asteroids.[9,10] Reference 11 used light curves and thermal emissions to recover the three-dimensional shape of an object assuming its orientation with respect to the observer is known. The benefits of using light curve data is that use of this approach is not limited to larger objects in lower orbits but can be applied to small and dim objects in higher orbits, such as geostationary. Here light curve data is considered for shape estimation, which is useful because it provides a mechanism to estimate both position and attitude, as well as the respective rates.[12,13]

There are several aspects of using light curve data (temporal photometry) that make it particularly advantageous for object detection, identification and tracking. Light curve data are the time-varying sensor wavelength-dependent apparent magnitude of energy (e.g. photons) scattered (reflected) off of an object along the line-of-sight to an observer. Because the apparent magnitude of the RSO is a function of its size,

orientation, and surface material properties, one or more of these characteristics should be recoverable from the photometric data. This can aid in the detection and identification of an RSO after a catalog of spacecraft data with material properties is developed, and may also prove to be powerful for never-seen-before objects. Determining the material properties of an object can also give insight into its surface instrumentation and equipment, i.e. solar panels or painted aluminum.

There is a coupling between RSO attitude and non-conservative accelerations. This can be exploited to assist in the estimation of the RSO trajectory. The measurement of the apparent magnitude is a function of several RSO characteristics that are those which drive certain non-conservative forces (i.e. solar radiation pressure (SRP)). The acceleration due to SRP is modeled as function of an object's Sun-facing area, surface properties and attitude. It has a very small magnitude compared to gravitational accelerations, and typically has an order of magnitude around 10^{-7} to 10^{-9} km/s^2, but is the dominant non-conservative acceleration for objects above 1,000 km. Below 1,000 km, drag caused by the atmospheric neutral density is the dominating non-conservative acceleration.

Filtering algorithms for state estimation, such as the extended Kalman filter (EKF),[14] the Unscented Kalman filter (UKF)[15] and particle filters (PFs)[16] are commonly used to both estimate hidden (indirectly observable) states and filter noisy measurements. The basic difference between the EKF and the UKF results from the manner in which the state distribution of the nonlinear models is approximated. The UKF, introduced by Julier and Uhlmann,[15] uses a nonlinear transformation called the unscented transform, in which the state probability distribution (pdf) is represented by a set of weighted sigma points (state vectors deterministically sampled about a mean). These are used to parameterize the true mean and covariance of the state distribution.

When the sigma points are propagated through the nonlinear system, the posterior mean and covariance are obtained up to the second order for any nonlinearity. The EKF and UKF assume that the process noise terms are represented by zero-mean Gaussian white-noise processes and the measurement noise is also represented by zero-mean Gaussian random variable. Furthermore both approaches assume that the *a posteriori* density function is Gaussian in a linear domain. This is true given the previous assumptions but under the effect of nonlinear measurement functions and system dynamics the initial Gaussian state uncertainty may quickly become non-Gaussian.

Both filters only provide approximate solutions to the nonlinear filtering problem, since the *a posteriori* density function is most often non-Gaussian due to nonlinear effects. The EKF typically works well only in the region where the first-order Taylor-series linearization adequately approximates the non-Gaussian probability density function (pdf). The UKF provides higher-order moments for the computation of the *a posteriori* pdf without the need to calculate Jacobian matrices as required in the EKF. The light curve measurement model is highly nonlinear and Jacobian calculations are non-trivial; thus, the UKF is used to provide a numerical means of estimating the states of the RSO using light curve measurement models.

Attitude estimation using light curve data has been demonstrated in Ref. 17. The main goal of this current work is to use light curve data to, autonomously and in near real-time, determine the shape of a RSO along with its attitude (rotational) and translational states. In order to accomplish this task a multiple-model adaptive estimation (MMAE) approach is used; running a number of parallel UKFs the MMAE approach determines the most probable shape of a RSO in orbit among a number of candidate shape models. Each filter uses a different assumed shape model, and the state estimate is given by the weighted sum of each filter's estimate. The weights correspond to the conditional probabilities derived from Bayes' rule using the likelihood information of the unknown states conditioned on the current-time measurement residual and innovations covariance. Several shapes are tested in a multiple hypothesis approach to assess the performance of the proposed method.

The organization of this paper is as follows. First, the models for RSO shape, orbital dynamics, and attitude dynamics are discussed. Then a description of the measurement models used in this paper are given. Next, a review of the UKF approach is provided. Following this, the MMAE structure is outlined and discussed. Finally, simulation results of the shape estimation approach are provided.

II. Shape Model Definition

The shape model considered in this work consists of a finite number a flat facets, where each facet has a set of basis vectors associated with it. These basis vectors are defined in Figure 1 and consist of three unit vectors $\mathbf{u}_n^B$, $\mathbf{u}_u^B$, and $\mathbf{u}_v^B$. The unit vector $\mathbf{u}_n^B$ points in the direction normal to the lighted facet. For

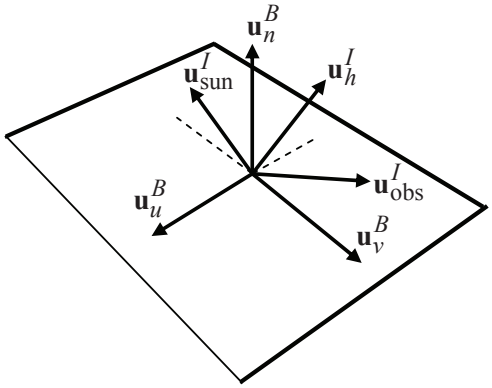

Figure 1. Geometry of Reflection

curved surfaces this model become more accurate as the number of facets are increased. The vectors $\mathbf{u}_u^B$ and $\mathbf{u}_v^B$ are in the plane of the facet, the notation superscript B denotes that the vector is expressed in body coordinates. The RSOs are assumed to be rigid bodies and therefore the unit vectors $\mathbf{u}_n^B$, $\mathbf{u}_u^B$ and $\mathbf{u}_v^B$ do not change since they are expressed in the body frame.

The light curve and the solar radiation pressure models discussed in the next sections require that these vectors be expressed in inertial coordinates and since the RSO body is rotating these vectors will change inertially. The body vectors can be rotated to the inertial frame by the standard attitude mapping given by:

$$\mathbf{u}_i^B = A(\mathbf{q}_I^B)\mathbf{u}_i^I, \quad i = u,\, v,\, n \tag{1}$$

where $A(\mathbf{q}_I^B)$ is the attitude matrix using the quaternion parameterization. Furthermore, the unit vector $\mathbf{u}_{\text{sun}}^I$ points in the Sun direction and the unit vector $\mathbf{u}_{\text{obs}}^I$ points from the object to the observer. The vector $\mathbf{u}_h^I$ is the normalized half vector between $\mathbf{u}_{\text{sun}}^I$ and $\mathbf{u}_{\text{obs}}^I$. This vector is also known as the Sun-RSO-Observer bisector. Each facet has an area A_j associated with it. Once the number of facets has been defined and their basis vectors are known, the areas A_j define the size and shape of the RSO. To determine the solar radiation pressure forces and light curve characteristics, the surface properties must be defined for each facet.

III. System Models

A. Orbital and Attitude System Model

In this paper the position and velocity of a Earth orbiting RSO are denoted by $\mathbf{r} = [x,\ y,\ z]^T$ and velocity $\mathbf{v} = [v_x,\ v_y,\ v_z]^T$ respectively. The Newtonian two-body gravitational equations of motion in Earth-centered inertial coordinates (ECI) are given by

$$\ddot{\mathbf{r}}^I = -\frac{\mu}{\|\mathbf{r}^I\|^3}\mathbf{r}^I + \mathbf{a}_{\text{srp,tot}}^I \tag{2}$$

where the terms μ represents the gravitational parameter of the Earth and $\mathbf{a}_{\text{srp,tot}}^I$ represents the acceleration perturbation due the solar radiation pressure, which will be discussed in detail in the following section.

A number of parameterizations exist to specify attitude, including Euler angles, quaternions, and Rodrigues parameters.[18] This paper uses the quaternion, which is based on the Euler angle/axis parametrization. The quaternion is defined as $\mathbf{q} \equiv \begin{bmatrix} \boldsymbol{\varrho}^T & q_4 \end{bmatrix}^T$ with $\boldsymbol{\varrho} = \begin{bmatrix} q_1 & q_2 & q_3 \end{bmatrix}^T = \hat{\mathbf{e}}\sin(\nu/2)$, and $q_4 = \cos(\nu/2)$, where $\hat{\mathbf{e}}$ and ν are the Euler axis of rotation and rotation angle, respectively. This vector must satisfy the constraint $\mathbf{q}^T\mathbf{q} = 1$. The attitude matrix can be written as a function of the quaternion:

$$A = \Xi^T(\mathbf{q})\Psi(\mathbf{q}) \tag{3}$$

where

$$\Xi(\mathbf{q}) \equiv \begin{bmatrix} q_4 I_{3\times 3} + [\boldsymbol{\varrho}\times] \\ -\boldsymbol{\varrho}^T \end{bmatrix} \tag{4a}$$

$$\Psi(\mathbf{q}) \equiv \begin{bmatrix} q_4 I_{3\times 3} - [\boldsymbol{\varrho}\times] \\ -\boldsymbol{\varrho}^T \end{bmatrix} \tag{4b}$$

and

$$[\mathbf{a}\times] = \begin{bmatrix} 0 & -a_3 & a_2 \\ a_3 & 0 & -a_1 \\ -a_2 & a_1 & 0 \end{bmatrix} \tag{5}$$

for any general 3×1 vector $\mathbf{a}$. The quaternion kinematics equation is given by

$$\dot{\mathbf{q}} = \frac{1}{2}\Xi(\mathbf{q})\boldsymbol{\omega} \tag{6}$$

where $\boldsymbol{\omega}$ is the angular velocity. The discrete-time form of the quaternion propagation is given by

$$\mathbf{q}_{k+1} = \bar{\Omega}(\boldsymbol{\omega}_k)\mathbf{q}_k \tag{7}$$

where

$$\bar{\Omega}(\boldsymbol{\omega}_k) \equiv \begin{bmatrix} \cos\left(\frac{1}{2}\|\boldsymbol{\omega}_k\|\Delta t\right) I_{3\times 3} - [\boldsymbol{\psi}_k\times] & \boldsymbol{\psi}_k \\ -\boldsymbol{\psi}_k^T & \cos\left(\frac{1}{2}\|\boldsymbol{\omega}_k\|\Delta t\right) \end{bmatrix} \tag{8a}$$

$$\boldsymbol{\psi}_k \equiv \frac{\sin\left(\frac{1}{2}\|\boldsymbol{\omega}_k\|\Delta t\right)\boldsymbol{\omega}_k}{\|\boldsymbol{\omega}_k\|} \tag{8b}$$

and Δt is the sampling interval. The discrete-time propagation equation can be used to simulate the attitude system kinematics and the two-body equation of motion can be integrated to account for the attitude-dependent solar radiation pressure given the attitude trajectory. It is important to note that the rotational dynamics can be much faster then the translational dynamics. If the trajectory is integrated as a 6-degree-of-freedom (6DOF) system, the propagation of the translational states is subject to the same integration time step Δt as the rotational dynamics. Therefore, care must be given to this subject. Typically, attitude and orbit determination and prediction are done separately unless the dynamics between the two are tightly coupled, as is the case with a RSO re-entering the Earth's atmosphere or say tethered RSOs. On short time scales, for the RSO trajectories that are considered here, the attitude and orbit dynamics are weakly coupled at best. However, for long-term predictions, the temporal rotational history is required to accurately account for all non-conservative forces (e.g. SRP) experienced by the RSO. The benefit of the information fusion gained from reducing both astrometric (angles) and photometric (light curve) data is that the photometry is sensitive to the same RSO characteristics that influence the non-conservative forces. The astrometric data are sensitive to RSO dynamic effects that integrate into the observed RSO position over time. However, these integrated dynamic effects (or dynamic signal) must be sufficiently observable above the astrometric data measurement noise and "integrated" implies latency in recovering these effects. The photometric data, on the other hand, are insensitive to the RSO integrated dynamic effect but rather sensitive to the instantaneous integrated characteristics effect (e.g. observed brightness as a function of the combined orientation, albedo area, and material properties). This facilitates the recovery of the RSO characteristics on much shorter time scales than required if it is relied solely upon the astrometric data.

B. Solar Pressure Model

The acceleration due to SRP is computed as a function of the total solar energy impressed upon exposed RSO surfaces that gets reflected, absorbed, and reradiated. The RSO albedo area is computed as

$$A_{\text{proj}} = A_{\text{sc}} \left|\cos(\theta_{\text{inc}})\right| \tag{9}$$

where θ_{inc} is the incident angle between the surface normal and the vector which points from the spacecraft to the Sun. The model from Ref. 19 describes the specular and diffuse composition of the solar radiation

pressure. The incoming energy flux is accounted for in three terms: the absorptive coefficient R_{abs}, the specular reflective coefficient R_{spec}, and the diffuse reflective coefficient R_{diff} allowing one to write:

$$R_{\text{abs}} + R_{\text{spec}} + R_{\text{diff}} = 1 \tag{10}$$

Reference 19 defines $\gamma = R_{\text{spec}} + R_{\text{diff}}$, which is the total reflectivity including the specular and the diffuse components. The average solar energy flux at 1 AU (energy flux through a sphere of radius 1 AU, centered at the Sun) is denoted by $C_{\text{sun,tot}} = 1367$ W/m^2. Therefore the energy flux at any distance d is given by $C_{\text{sun,tot}}/(d/d_0)^2$ where $d_0 = 1$ AU. The momentum of a photon is equal to the energy divided by the speed of light c. The pressure force is the divided into a specularly reflected radiated component, diffusively radiated component, and a thermal emissive component from the energy absorbed and reradiated. The pressure force is then converted to an acceleration by dividing the force by the mass of the RSO, which denoted by m_{RSO}. From this, the acceleration due to SRP in inertial coordinates is calculated:

$$\mathbf{a}^I_{\text{srp}} = \frac{-C_{\text{sun,tot}} A_{\text{proj}}}{c\, m_{RSO} (d/d_0)^2} \left(B_{\text{srp}} \mathbf{u}^I_n + (1 - 2\mu_{\text{srp}}) \cos(\theta_{\text{inc}}) \mathbf{u}^I_{\text{sun}} \right) \tag{11}$$

where

$$\beta_{\text{srp}} = \frac{R_{\text{spec}}}{R_{\text{diff}} + R_{\text{spec}}} \tag{12a}$$

$$\nu_{\text{srp}} = \frac{1}{3} \left[(1 - \beta_{\text{srp}}) \gamma_{\text{srp}} + \epsilon_{\text{srp}} (1 - \gamma_{\text{srp}}) \right] \tag{12b}$$

$$\mu_{\text{srp}} = \frac{1}{2} \beta_{\text{srp}} \gamma_{\text{srp}} \tag{12c}$$

$$B_{\text{srp}} = 2\nu_{\text{srp}} \cos(\theta_{\text{inc}}) + 4\mu_{\text{srp}} \cos^2(\theta_{\text{inc}}) \tag{12d}$$

$$\tag{12e}$$

where ϵ_{srp} is the emissivity. Note that due to Eq. (10) the value for R_{abs} is not required for the SRP model given in Eq. (11). The sum of these accelerations is taken to be the total acceleration due to SRP on the RSO:

$$\mathbf{a}^I_{\text{srp,tot}} = \sum_{j=1}^{6} \mathbf{a}^I_{\text{srp},j} \tag{13}$$

The sum is preformed over all sides of the RSO. If for any side the angle between the surface normal and the Sun's direction is greater than π then this side is not facing the Sun and receives no energy form the Sun. Therefore the solar radiation pressure for these sides is set to zero, $\mathbf{a}^I_{\text{srp},j} =$ if $\theta_{\text{inc}} > \pi$.

IV. Observation Model

A. Astrometric Observation Model

Consider observations made by a optical site which measures azimuth and elevation to a RSO. The geometry and common terminology associated with this observation is shown in Figure 2, where $\boldsymbol{\rho}$ is the slant range, $\mathbf{r}$ is the radius vector locating the RSO, $\mathbf{R}$ is the radius vector locating the observer, α and δ is the right ascension and declination of the RSO, respectively, θ is the sidereal time of the observer, λ is the latitude of the observer, and ϕ is the east longitude from the observer to the spacecraft. The fundamental observation is given by

$$\boldsymbol{\rho} = \mathbf{R} - \mathbf{r} \tag{14}$$

In non-rotating equatorial (inertial) components the vector $\boldsymbol{\rho}$ is given by

$$\boldsymbol{\rho} = \begin{bmatrix} x - ||\mathbf{R}|| \cos(\theta) \cos(\lambda) \\ y - ||\mathbf{R}|| \cos(\lambda) \sin(\theta) \\ z - ||\mathbf{R}|| \sin(\lambda) \end{bmatrix} \tag{15}$$

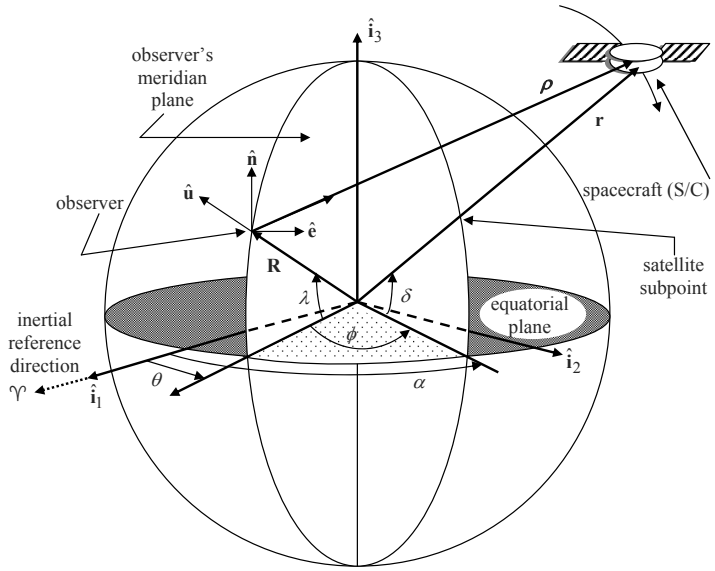

Figure 2. Geometry of Earth Observations of Spacecraft Motion

where x, y, and z are the components of the vector $\mathbf{r}$. The conversion from the inertial to the observer coordinate system (Up-East-North) is given by

$$\begin{bmatrix} \rho_u \\ \rho_e \\ \rho_n \end{bmatrix} = \begin{bmatrix} \cos(\lambda) & 0 & \sin(\lambda) \\ 0 & -1 & 0 \\ -\sin(\lambda) & 0 & \cos(\lambda) \end{bmatrix} \begin{bmatrix} \cos(\theta) & \sin(\theta) & 0 \\ -\sin(\theta) & \cos(\theta) & 0 \\ 0 & 0 & -1 \end{bmatrix} \boldsymbol{\rho} \tag{16}$$

Next, consider a radar site that measures the azimuth, Θ, and elevation, Φ. The observation equations are given by

$$\Theta = \tan^{-1}\left(\frac{\rho_e}{\rho_n}\right) \tag{17a}$$

$$\Phi = \sin^{-1}\left(\frac{\rho_u}{||\boldsymbol{\rho}||}\right) \tag{17b}$$

The apparent magnitude will also be employed along with the azimuth and elevation, which will be described next.

B. Light Curve Observation Model

The brightness of an object in space can be modeled using an anisotropic Phong light diffusion model.[20] This model is based on the bidirectional reflectance distribution function (BRDF) which models light distribution scattered from the surface due to the incident light. The BRDF at any point on the surface is a function of two directions, the direction from which the light source is originating from and the direction from which the scattered light leaves the observed the surface. The model in Ref. 20 decomposes the BRDF into a specular component and a diffuse component. The two terms sum to give the total BRDF:

$$\rho_{\text{total}} = \rho_{\text{spec}} + \rho_{\text{diff}} \tag{18}$$

The diffuse component represents light that is scattered equally in all directions (Lambertian) and the specular component represents light that is concentrated about some direction (mirror-like). Reference 20 develops a model for continuous arbitrary surfaces but simplifies for flat surfaces. This simplified model is employed in this work and shape models are considered that consist of a finite number of flat facets. Therefore the total observed brightness of an object becomes the sum of the contribution from each facet.

Under these assumptions the specular term of the BRDF becomes[20]

$$\rho_{\text{spec}} = \frac{\sqrt{(n_u+1)(n_v+1)}}{8\pi} \frac{\left(\mathbf{u}_n^I \cdot \mathbf{u}_h^I\right)^z}{(\mathbf{u}_h^I \cdot \mathbf{u}_{\text{sun}}^I)\max(\mathbf{u}_n^I \cdot \mathbf{u}_{\text{sun}}^I,\, \mathbf{u}_n^I \cdot \mathbf{u}_{\text{obs}}^I)} F_{\text{reflect}} \tag{19a}$$

$$z = \frac{n_u(\mathbf{u}_h^I \cdot \mathbf{u}_u^I)^2 + n_v(\mathbf{u}_h^I \cdot \mathbf{u}_v^I)^2}{1-(\mathbf{u}_n^I \cdot \mathbf{u}_{\text{sun}}^I)^2} \tag{19b}$$

The parameters of the Phong model that dictate the direction (locally horizontal or vertical) distribution of the specular terms are n_u and n_v. The terms in Eq. (19) are functions of the reflection geometry which is described in Figure 1. The diffuse term of the BRDF is

$$\rho_{\text{diff}} = \left(\frac{28R_{\text{diff}}}{23\pi}\right)(1-R_{\text{spec}})\left[1-\left(1-\frac{\mathbf{u}_n^I \cdot \mathbf{u}_{\text{sun}}^I}{2}\right)^5\right]\left[1-\left(1-\frac{\mathbf{u}_n^I \cdot \mathbf{u}_{\text{obs}}^I}{2}\right)^5\right] \tag{20}$$

The apparent magnitude of a RSO is the result of sunlight reflecting off of its surfaces along the line-of-sight to an observer. First, the fraction of visible sunlight that strikes an object (and not absorbed) is computed by combining Eq. (18) with

$$F_{\text{sun}} = C_{\text{sun,vis}}\, \rho_{\text{total}}\, \mathbf{u}_n^I \cdot \mathbf{u}_{\text{sun}}^I \tag{21}$$

where $C_{\text{sun,vis}} = 455$ W/m^2 is the power per square meter impinging on a given object due to visible light striking the surface. If either the angle between the surface normal and the observer's direction or the angle between the surface normal and Sun direction is greater than π then there is no light reflected toward the observer. If this is the case then the fraction of visible light is set to $F_{\text{sun}} = 0$. Next, the fraction of sunlight that strikes an object that is reflected must be computed. Here, F_{sun} is used:

$$F_{\text{obs}} = \frac{F_{\text{sun}} A_{\text{sc}} \mathbf{u}_n^I \cdot \mathbf{u}_{\text{obs}}^I}{||\mathbf{r}_{\text{obs}}||^2} \tag{22}$$

where $\mathbf{r}_{\text{obs}}$ is the position vector of the observer. The surface area of one facet of a spacecraft's surface is denoted by A_{sc}. The reflected light is now used to compute the apparent magnitude, which is measured by an observer:

$$m_{\text{app}} = -26.7 - 2.5\log_{10}\left|\frac{F_{\text{obs}}}{C_{\text{sun,vis}}}\right| \tag{23}$$

where -26.7 is the apparent magnitude of the sun. With the spacecraft defined as in §VII, the apparent magnitude of all sides is computed and the value corresponding to the brightest magnitude is accepted as the magnitude measurement.

V. Unscented Filtering Using Light Curve Data

The Unscented Kalman filter (UKF) is chosen for state estimation because it has at least the accuracy of a second-order filter[15] without the requirement of computing Jacobians unlike the EKF. The UKF structure is used for estimating rotational and translational states based on fusing angles and light curve data along with their associated models as discussed §III. The attitude UKF described in Ref. 21 is used in the same manner as the one shown in Refs. 12 and 17. The global parameterization in the attitude UKF is the quaternion while a minimal parameterization involving the generalized Rodrigues parameters (GRPs) is used to define the local error. Quaternions are useful because their kinematics are free of singularities. The representation of the attitude error as a GRP is useful for the propagation and update stages of the attitude covariance because the structure of the UKF can be used directly. Complete explanations of the quaternion and its mapping to GRPs is provided in Refs. 22 and 23. The angle data can be used to determine the unknown position and velocity of a RSO but if the position is coupled with the attitude dynamics then angle data can assist with attitude estimation as well. However if position is known accurately, then using only light curve data is sufficient to determine the shape in the MMAE process.

A UKF is now summarized for estimating the state of an RSO's position, velocity, orientation and rotation rate given by $\mathbf{x} = [\mathbf{q}_I^{B^T}\ \boldsymbol{\omega}_{B/I}^{B^T}\ \mathbf{r}^{I^T}\ \mathbf{v}^{I^T}]^T$, where $\mathbf{q}_I^B$, where $\boldsymbol{\omega}_{B/I}^B$ is the angular velocity of the body frame with respect to the inertial frame expressed in body coordinates. The standard orbit model in Eq. (2) can be written in the general state equation which gives the deterministic part of the stochastic model:

$$\dot{\mathbf{x}} = \mathbf{f}(\mathbf{x}, t) + G(\mathbf{x}, t)\,\boldsymbol{\Gamma}(t) \tag{24}$$

where $\mathbf{\Gamma}(t)$ is a Gaussian white noise process term with correlation function $Q\delta(t_1 - t_2)$. The function $\mathbf{f}(\mathbf{x}, t)$ is a general nonlinear function. To solve the general nonlinear filtering problem the UKF utilizes the unscented transformation to determine the mean and covariance propagation though the function $\mathbf{f}(\mathbf{x}, t)$. If the initial pdf $p(\mathbf{x}_o)$ that describes the associated state uncertainty is given, the solution for the time evolution of $p(\mathbf{x}, t)$ constitutes the nonlinear filtering problem.

Given a system model with initial state and covariance values, the UKF propagates the state vector and the error-covariance matrix recursively. At discrete observation times, the UKF updates the state and covariance matrix conditioned on the information gained by the measurement. The prediction phase is important for overall filter performance. In general, the discrete measurement equation can be expressed for the filter as

$$\tilde{\mathbf{y}}_k = \mathbf{h}(\mathbf{x}_k) + \mathbf{v}_k \tag{25}$$

where $\tilde{\mathbf{y}}_k$ is a measurement vector and $\mathbf{v}_k$ is the measurement noise, which is assumed to be a zero-mean Gaussian process with covariance R_k.

All random variables in the UKF are assumed to be Gaussian random variables and their distribution is approximated by the deterministically selected sigma points. The sigma points are selected to be along the principal axis direction of the assumed Gaussian state distribution or along the eigenvector directions of the state error-covariance, P. Given an $n \times n$ covariance matrix P_k, the sigma points are constructed by

$$\boldsymbol{\sigma}_k \leftarrow 2n \text{ columns from } \sqrt{(n+\lambda)P_k} \tag{26a}$$

$$\boldsymbol{\chi}_k(0) = \boldsymbol{\mu}_k \tag{26b}$$

$$\boldsymbol{\chi}_k(i) = \boldsymbol{\sigma}_k(i) + \boldsymbol{\mu}_k \tag{26c}$$

where $\sqrt{M}$ is shorthand notation for a matrix Z such that $M = Z\,Z^T$. Then given that these points are selected to represent the distribution of the state vector, each sigma point is given a weight that preserves the information contained in the initial distribution:

$$W_0^{\text{mean}} = \frac{\lambda}{n+\lambda} \tag{27a}$$

$$W_0^{\text{cov}} = \frac{\lambda}{n+\lambda} + (1 - \alpha^2 + \beta) \tag{27b}$$

$$W_i^{\text{mean}} = W_i^{\text{cov}} = \frac{1}{2(n+\lambda)}, \quad i = 1,\, 2,\, \ldots,\, 2n \tag{27c}$$

where $\lambda = \alpha^2 n + \kappa - n_a$ includes scaling parameters. The constant parameter controls the size of the sigma point distribution and should be a small number $0 \leq \alpha \leq 1$, and κ provides an extra degree of freedom that is used to fine-tune the higher-order moments; $\kappa = 3 - n$ for a Gaussian distribution, also β is a third parameter that further incorporates higher-order effects by adding the weighting of the zeroth sigma point to the calculation of the covariance; note $\beta = 2$ is the optimal value for Gaussian distributions. The state vector for the joint attitude and position estimate problem is given by

$$\hat{\mathbf{x}}_k = \left[\begin{array}{c} \boldsymbol{\delta}\hat{\mathbf{p}}^- \\ \hat{\boldsymbol{\omega}}_{B/I}^{B-} \\ \hat{\mathbf{r}}^{I-} \\ \hat{\mathbf{v}}^{I-} \end{array} \right]\Bigg|_{t_k} \tag{28}$$

where $\boldsymbol{\delta}\hat{\mathbf{p}}$ is the error GRP state and $\hat{}$ is used to denote estimate. The initial estimate $\hat{\mathbf{x}}_0$ is the mean sigma point and is denoted $\boldsymbol{\chi}_0(0)$. The error GRP state of the initial estimate is set to zero, while the rest of the states are initialized by their respective initial estimates.

A. Predictor

The attitude state errors are represented as error GRPs resulting in a minimum parameter representation for the attitude state error.[21] Therefore the attitude state error-covariance can be directly decomposed into error GRPs sigma points and used in the UKF structure. Then sigma points corresponding to the error

GRPs are converted to full quaternions to compute the output estimate and propagate the sigma points. The error quaternion, denoted by $\boldsymbol{\delta}\mathbf{q}$, associated with the i^{th} error GRP sigma point is computed by[21]

$$\boldsymbol{\delta\varrho}_k^-(i) = f^{-1}\left[a + \delta q_{4_k}^-(i)\right]\boldsymbol{\chi}_k^{\delta p}(i) \tag{29a}$$

$$\delta q_{4_k}^-(i) = \frac{-a||\boldsymbol{\chi}_k^{\delta p}(i)||^2 + f\sqrt{f^2 + (1-a^2)||\boldsymbol{\chi}_k^{\delta p}(i)||^2}}{f^2 + ||\boldsymbol{\chi}_k^{\delta p}(i)||^2} \tag{29b}$$

$$\boldsymbol{\delta}\mathbf{q}_k^-(i) = \begin{bmatrix} \boldsymbol{\delta\varrho}_k^-(i) \\ \delta q_{4_k}^-(i) \end{bmatrix} \tag{29c}$$

where a is a parameter from 0 to 1 and f is a scale factor, which is often set to $f = 2(a+1)$. Here it will be noted that the subscript I and superscript B in $\mathbf{q}_I^B$ is omitted in this section for brevity. The representation of the attitude estimate perturbed by the i^{th} error quaternion is computed using the quaternion composition of the i^{th} error quaternion with the attitude estimate:

$$\hat{\mathbf{q}}_k^-(i) = \boldsymbol{\delta}\mathbf{q}_k^-(i) \otimes \hat{\mathbf{q}}_k^- \tag{30}$$

where

$$\mathbf{q}' \otimes \mathbf{q} = \begin{bmatrix} \Psi(\mathbf{q}') & \mathbf{q}' \end{bmatrix}\mathbf{q} \tag{31}$$

The sigma points are propagated through the quaternion kinematics and position dynamics:

$$\dot{\boldsymbol{\chi}}(i) = \mathbf{f}\left([\boldsymbol{\chi}(i), \hat{\mathbf{q}}(i)]\right) \tag{32}$$

where

$$\mathbf{f}\left([\boldsymbol{\chi}, \hat{\mathbf{q}}]\right) = \begin{bmatrix} \frac{1}{2}\Xi(\mathbf{q})\boldsymbol{\omega} \\ \mathbf{0} \\ \dot{\mathbf{r}}^I \\ -\frac{\mu}{||\mathbf{r}^I||^3}\mathbf{r}^I + \mathbf{a}_{\text{SRP}}^I \end{bmatrix} \tag{33}$$

The acceleration due to solar radiation pressure, $\mathbf{a}_{\text{srp}}^I$, is calculated with Eq. (11). After the propagation of the UKF, the sigma points and covariance are recomputed. In this case, the sigma points for the error GRP states are computed with the propagated attitude sigma points. The estimated mean sigma point quaternion, $\mathbf{q}_{k+1}^-(0)$, is stored, and error quaternions corresponding to each propagated quaternion sigma point are computed through the quaternion composition:

$$\boldsymbol{\delta}\mathbf{q}_{k+1}^-(i) = \hat{\mathbf{q}}_{k+1}^-(i) \otimes \left[\hat{\mathbf{q}}_{k+1}^-(0)\right]^{-1} \tag{34}$$

where the notation for the inverse quaternion is defined as:

$$\mathbf{q}^{-1} \equiv \begin{bmatrix} -\boldsymbol{\varrho} \\ q_4 \end{bmatrix} \tag{35}$$

Using the result of Eq. (34), the error GRP sigma points are computed as

$$\boldsymbol{\delta}\mathbf{p}_{k+1}^-(i) = f\frac{\boldsymbol{\delta}\hat{\boldsymbol{\varrho}}_{k+1}^-(i)}{a + \delta\hat{q}_{4_{k+1}}^-(i)} \tag{36}$$

The non-attitude sigma points are the propagated non-attitude states, and are assembled with the error GRP sigma points. Next, the mean is calculated as a weighted sum of the sigma points:

$$\hat{\mathbf{x}}_{k+1}^- = \sum_{i=0}^{2n} W_i^{\text{mean}}\,\boldsymbol{\chi}_{k+1}(i) \tag{37}$$

From which the predicted covariance is computed as:

$$P_{k+1}^- = \sum_{i=0}^{2n} W_i^{\text{cov}}\left[\boldsymbol{\chi}_{k+1}(i) - \hat{\mathbf{x}}_{k+1}^-\right]\left[\boldsymbol{\chi}_{k+1}(i) - \hat{\mathbf{x}}_{k+1}^-\right]^T + Q_{k+1} \tag{38}$$

where Q_{k+1} is the process noise covariance. Using the predicted covariance, P_{k+1}^-, a new spread of sigma points is computed using Eq. (26) and the cycle repeats for the next set of measurements.

B. Corrector

In this approach, the observation vector is composed of the apparent magnitude, azimuth and elevation:

$$\tilde{\mathbf{y}}_k = \mathbf{h}(\mathbf{x}_k) + \mathbf{v}_k \equiv \begin{bmatrix} m_{\text{app}} \\ \Theta \\ \Phi \end{bmatrix} + \mathbf{v}_k \tag{39}$$

where $\mathbf{v}_k$ is the measurement noise vector with covariance R_k. Using the full quaternions corresponding to the sigma points and the non-attitude sigma points, outputs corresponding to each sigma point are computed using magnitude and azimuth and elevation angle models previously. The outputs corresponding to the i^{th} sigma point are computed with Eq. (39):

$$\boldsymbol{\gamma}_k(i) = \mathbf{h}\left[\boldsymbol{\chi}_k(i), \hat{\mathbf{q}}_k^-\right] \tag{40}$$

Next the output estimate is computed with the weights described in Eqs. (27):

$$\hat{\mathbf{y}}_k^- = \sum_{i=0}^{2n} W_i^{\text{mean}}\, \boldsymbol{\gamma}_k(i) \tag{41}$$

The output, innovations and cross-correlation covariance are computed as

$$P_k^{yy} = \sum_{i=0}^{2n} W_i^{\text{cov}} \left[\boldsymbol{\gamma}_k(i) - \hat{\mathbf{y}}_k^-\right] \left[\boldsymbol{\gamma}_k(i) - \hat{\mathbf{y}}_k^-\right]^T \tag{42a}$$

$$P_k^{\upsilon\upsilon} = P_k^{yy} + R_k \tag{42b}$$

$$P_k^{xy} = \sum_{i=0}^{2n} W_i^{\text{cov}} \left[\boldsymbol{\chi}_k(i) - \hat{\mathbf{x}}_k^-\right] \left[\boldsymbol{\gamma}_k(i) - \hat{\mathbf{y}}_k^-\right]^T \tag{42c}$$

Next the gain is computed using

$$K_k = P_k^{xy} (P_k^{\upsilon\upsilon})^{-1} \tag{43}$$

and the estimate update is computed from

$$\hat{\mathbf{x}}_k^+ = \hat{\mathbf{x}}_k^- + K_k \left[\tilde{\mathbf{y}}_k - \hat{\mathbf{y}}_k\right] \tag{44}$$

After each update the error GRP states are set to zero:

$$\boldsymbol{\delta}\hat{\mathbf{p}}_k^+ = \mathbf{0} \tag{45}$$

The attitude update is performed by converting the first three states of the update to an error quaternion, $\boldsymbol{\delta}\hat{\mathbf{q}}_k$, and rotating the current quaternion attitude estimate by the result:

$$\hat{\mathbf{q}}_k^+ = \boldsymbol{\delta}\hat{\mathbf{q}}_k \otimes \hat{\mathbf{q}}_k^- \tag{46}$$

VI. Multiple-Model Adaptive Estimation

In this section a review of MMAE is shown. More details can be found in Refs. 24 and 25. Figure 3 shows the MMAE process. Multiple-model adaptive estimation is a recursive estimator that uses a bank of filters that depend on models with different parameters, denoted by the vector $\mathbf{p}$, which is assumed to be constant (at least throughout the interval of adaptation). Note the stationary assumption for the state and/or output processes is not necessarily required though, i.e. time varying state and output matrices can be used. A set of distributed elements is generated from some known pdf of $\mathbf{p}$, denoted by $p(\mathbf{p})$, to give $\{\mathbf{p}^{(\ell)};\, \ell = 1, \ldots, M\}$. The goal of the estimation process is to determine the conditional pdf of the ℓ^{th} element $\mathbf{p}^{(\ell)}$ given all the measurements.

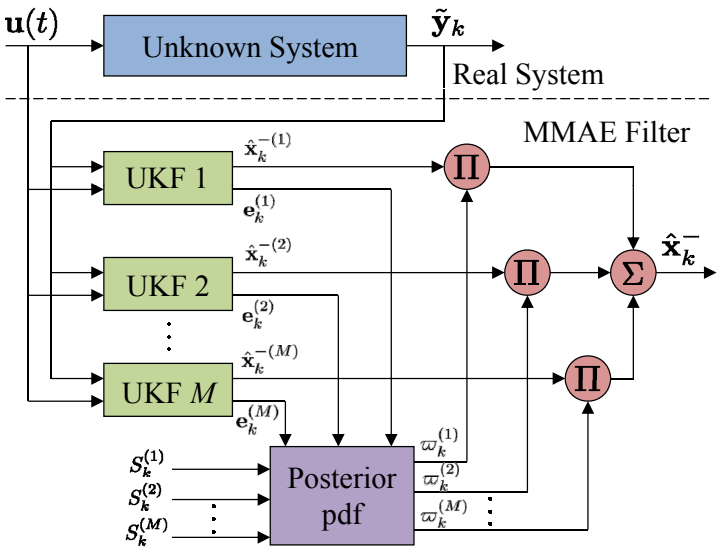

Figure 3. MMAE Process

Application of Bayes' rule yields

$$p\left(\mathbf{p}^{(\ell)}|\tilde{\mathbf{Y}}_k\right) = \frac{p\left(\tilde{\mathbf{Y}}_k|\mathbf{p}^{(\ell)}\right)p\left(\mathbf{p}^{(\ell)}\right)}{\sum_{j=1}^{M} p\left(\tilde{\mathbf{Y}}_k|\mathbf{p}^{(j)}\right)p\left(\mathbf{p}^{(j)}\right)} \tag{47}$$

where $\tilde{\mathbf{Y}}_k$ denotes the sequence $\{\tilde{\mathbf{y}}_0, \tilde{\mathbf{y}}_1, \ldots, \tilde{\mathbf{y}}_k\}$. The conditional probability $p\left(\mathbf{p}^{(\ell)}|\tilde{\mathbf{Y}}_k\right)$ will be the metric used to select the most likely model and or the most likely combination of shape models. The *a posteriori* probabilities can be computed through[26]

$$\begin{aligned} p\left(\mathbf{p}^{(\ell)}|\tilde{\mathbf{Y}}_k\right) &= \frac{p\left(\tilde{\mathbf{y}}_k, \mathbf{p}^{(\ell)}|\tilde{\mathbf{Y}}_{k-1}\right)}{p\left(\tilde{\mathbf{y}}_k|\tilde{\mathbf{Y}}_{k-1}\right)} \\ &= \frac{p\left(\tilde{\mathbf{y}}_k|\hat{\mathbf{x}}_k^{-(\ell)}\right)p\left(\mathbf{p}^{(\ell)}|\tilde{\mathbf{Y}}_{k-1}\right)}{\sum_{j=1}^{M}\left[p\left(\tilde{\mathbf{Y}}_k|\hat{\mathbf{x}}_k^{-(j)}\right)p\left(\mathbf{p}^{(j)}|\tilde{\mathbf{Y}}_{k-1}\right)\right]} \end{aligned} \tag{48}$$

The conditional probability densities of the observations based on each hypothesis (likelihood) $p\left(\tilde{\mathbf{y}}_k|\hat{\mathbf{x}}_k^{-(\ell)}\right)$ are given as

$$p\left(\tilde{\mathbf{y}}_k|\hat{\mathbf{x}}_k^{-(\ell)}\right) = \frac{1}{(2\pi)^{m/2}|S_k^{(\ell)}|^{1/2}} e^{-(1/2)\mathbf{e}_k^{(\ell)T} S_k^{(\ell)} \mathbf{e}_k^{(\ell)}} \tag{49}$$

where n is the dimension of the residual state and measurement residual is defined by

$$\mathbf{e}_k^{(\ell)} = \tilde{\mathbf{y}}_k - \mathbf{h}[\hat{\mathbf{x}}_k^{-}(\mathbf{p}^{(\ell)})] \tag{50}$$

and corresponding residual covariance matrix from the UKF

$$S_k^{(i)} = P_k^{vv} \tag{51}$$

Table 1. RSO Geometry for Proposed Models

RSO	Surface Area of Model
Model 1 (true model)	30 30 80 80 80 80 m^2
Model 2	20 20 50 50 50 50 m^2
Model 3	30 30 100 50 100 50 m^2
Model 4	0.5 0.5 80 0.5 80 0.5 m^2
Model 5	50 50 50 50 50 50 m^2

where P_k^{vv} is given by Eq. (42b) using the i^{th} filter.

Note that the denominator of Eq. (48) is just a normalizing factor to ensure that $p\left(\mathbf{p}^{(\ell)}|\tilde{\mathbf{Y}}_k\right)$ is a pdf. The recursion formula can now be cast into a set of defined weights $\varpi_k^{(\ell)}$, so that

$$\begin{aligned} \varpi_k^{(\ell)} &= \varpi_{k-1}^{(\ell)} p\left(\tilde{\mathbf{y}}_k|\hat{\mathbf{x}}_k^{-(\ell)}\right) \\ \varpi_k^{(\ell)} &\leftarrow \frac{\varpi_k^{(\ell)}}{\sum_{j=1}^{M} \varpi_k^{(j)}} \end{aligned} \tag{52}$$

where $\varpi_k^{(\ell)} \equiv p\left(\mathbf{p}^{(\ell)}|\tilde{\mathbf{y}}_k\right)$. Note that only the current time measurement $\tilde{\mathbf{y}}_k$ is needed to update the weights. The weights at time t_0 are initialized to $\varpi_0^{(\ell)} = 1/M$ for $\ell = 1, 2, \ldots, M$. The convergence properties of MMAE are shown in Ref. 26, which assumes ergodicity in the proof. The ergodicity assumptions can be relaxed to asymptotic stationarity and other assumptions are even possible for non-stationary situations.[27]

VII. Simulation Results

Two simulations scenarios are presented: one where the true model is considered in the filter bank and one where true model is not in the bank but is a combination of two of the models. In both cases the same dynamic configuration is considered, with same initial attitude, true orbit and true angular velocity. For the generation of data for the true model, an equatorial ground station is chosen as the site of the observer. The RSO is simulated to fly in a near-geosynchronous orbit in a continuously-lighted trajectory. This is accomplished by inclining the orbit by 15 degrees and choosing an appropriate time of the year, thereby avoiding the shadow cast by the Earth.

The initial inertial position and velocity are chosen as $\mathbf{r}^I = [-2.8 \times 10^3 \;\; 2.8 \times 10^3 \;\; 0]^T$ km and $\mathbf{v}^I = [-1.5511 \;\; -1.5511 \;\; 2.1936]^T$ km/s. The geographic position of the ground site is 0° North, 172° West with 0 km altitude. The time of the start of the simulation is May 8, 2007 at 5:27.55. The initial true quaternion attitude mapping from the inertial frame to the body frame is chosen as $\mathbf{q}_I^B = [1/2 \;\; 0 \;\; 0 \;\; 1/2]^T$. A constant rotation rate, defined as the body rate with respect to the inertial frame, represented in body coordinates, is used given by $\boldsymbol{\omega}_{B/I}^B = [0 \;\; 0 \;\; 0.0262]^T$ rad/s.

For both simulations scenarios, measurements are produced using zero-mean white-noise error processes with standard deviation of 0.1 for magnitude and standard deviation of 2 arc-seconds for azimuth and elevation. The initial errors for the states are 5 deg for all three attitudes, 1,000 deg/hr for the rotational rates, and 100 km and 0.1 km/s for the position and the velocity errors, respectively. The initial condition error-covariance values are set to 20^2 deg^2 for all three attitudes, $1,400^2$ $(\text{deg/hr})^2$ for the rotational rates, 100^2 km^2 and 0.1^2 $(\text{km/s})^2$ for the position and the velocity errors, respectively. The time interval between the measurements is set to 30 seconds.

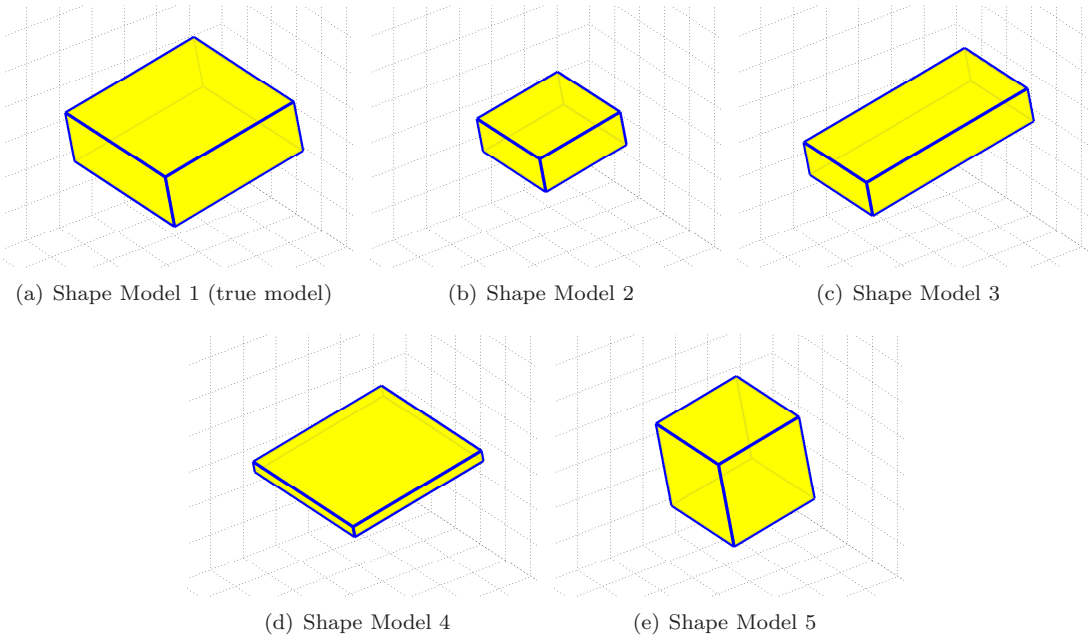

(a) Shape Model 1 (true model) (b) Shape Model 2 (c) Shape Model 3

(d) Shape Model 4 (e) Shape Model 5

Figure 4. RSO Shape Hypothesis for Scenario I

A. Scenario I: True Model Exists in Filter Bank

For the development of the measured light curve data a six-faceted RSO is used. For the truth model four facets have an area of 80 m^2 and the other two have an area of 30 m^2 These parameters, along with the geometries of the other four assumed models, are shown in Table 1 and Figure 4. The mass for the true RSO is selected to be $m_{RSO} = 1000$ kg, which gives a maximum area-to-mass ratio of 0.08 for this model. The other models are selected to have a mass of 1000 kg as well. It should be noted that the mass does not introduce a new model parameter but rather the important quantity is really the area-to-mass ratio. The Phong specularity parameters, n_u and n_v,[20] are chosen to be 10 for each facet to yield realistic visible magnitude. Two large facets and one small facet have reflectance values of $R_{\text{spec}} = 0.7$ and $R_{\text{diff}} = 0.3$, and reflect more light than the other three. The other three facets have the following values: $R_{\text{spec}} = 0.2$, and $R_{\text{diff}} = 0.1$. The reflectance of the other four models are the same as the true model. The attitude and reflectance estimation depends on the observability in terms of changes in magnitude. Therefore sides of different size and reflectance are chosen to increase observability.

The initial probabilities for the MMAE algorithm of all three models are set to 1/5, so each model is weighted equally at the beginning of the MMAE process. The calculated probabilities over time from the MMAE algorithm for each model are shown in Figure 5. In the beginning of the simulation time, when the first measurements are received, the MMAE algorithm determines Model 2 to be the most probable model, but after a few more measurements are received (at around $t = 15$ minutes or 30 measurements), the conditional probability of Model 1, which is the true model, converges to near one, while the conditional probabilities of the other models go to near zero. The estimation errors, along with their respective 3σ bounds calculated from the covariance of the UKF, for attitude, position, velocity and rotation rate are shown in Figures 6. The attitude is estimated to within 1° of uncertainty, and attitude rate is found to within 1 deg/hr. Position and velocity are estimated to within 200 km and 0.02 km/s, respectively. All states show proper filter convergence behavior in that the residual errors settle down and are bounded by their computed 3σ bounds.

B. Scenario II: True Model is the Combination of Two Models

In the second simulation scenario the truth model is chosen such that it shape resembles two of the models given to MMAE filter bank but the exact true shape model is not in the MMAE filter bank. The four facets have areas of the true model are 80 m^2 for two, 60 m^2 for two, the other two have an area of 50 m^2. These

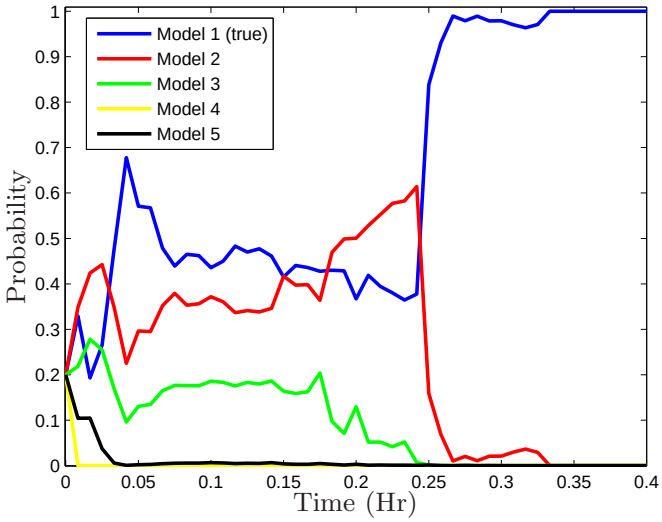

Figure 5. MMAE Consisting of Five RSO Models

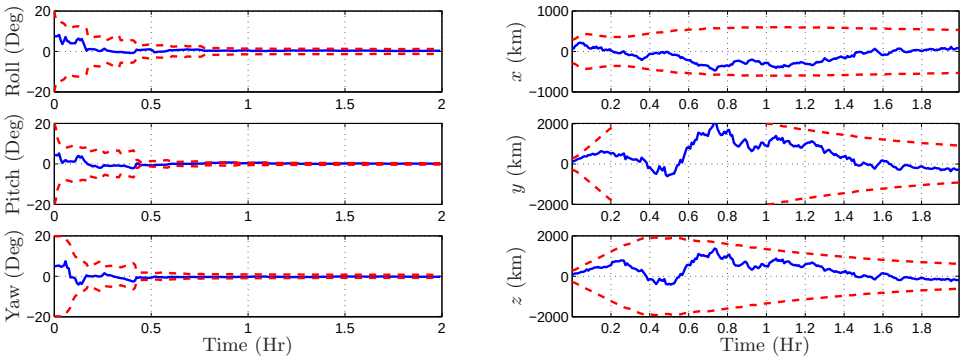

(a) Attitude Estimation Error

(b) Position Estimation Error

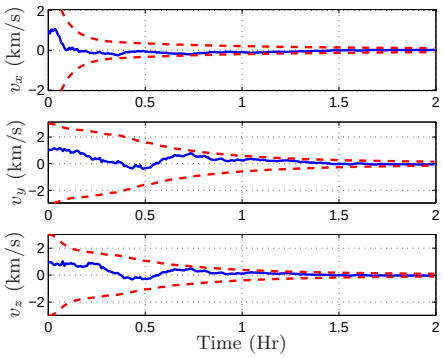

(c) Velocity Estimation Error

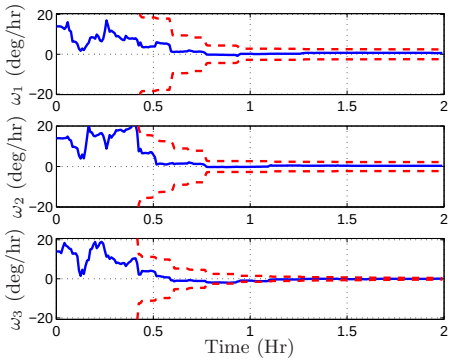

(d) Angular Velocity Estimation Error

Figure 6. RSO State Estimation Results

parameters, along with the geometries of the other assumed models, are shown in Table 2 and Figure 7. Note that the true model shape is close to models one and five. The Phong specularity parameters, n_u and n_v, and the masses of each model are chosen to be same as the previous example.

The initial probabilities for the MMAE algorithm of all three models are set to 1/5, so each model is

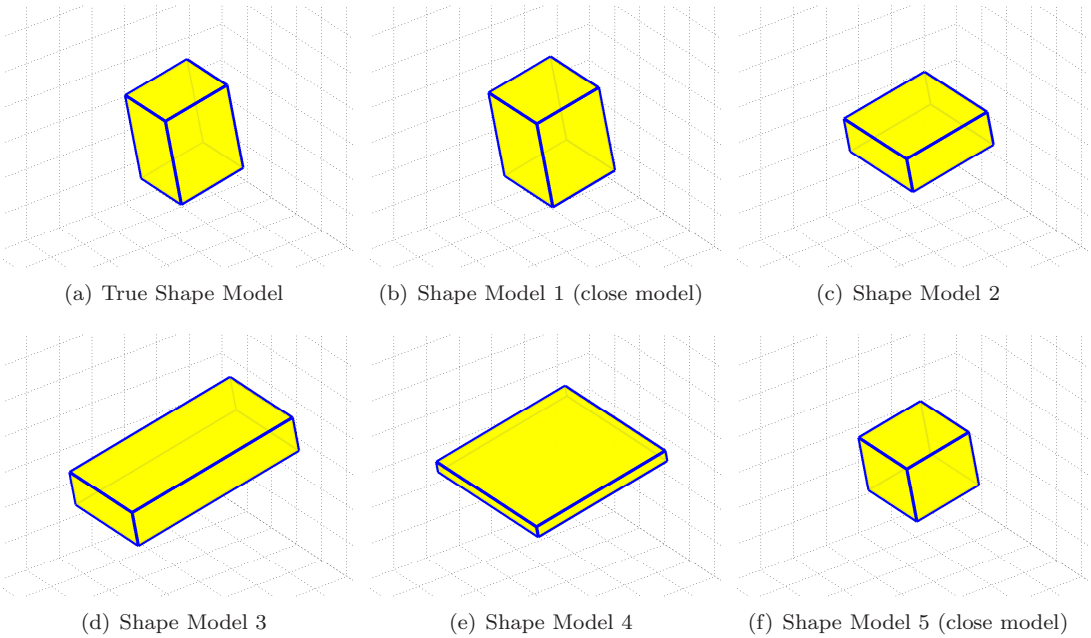

(a) True Shape Model (b) Shape Model 1 (close model) (c) Shape Model 2

(d) Shape Model 3 (e) Shape Model 4 (f) Shape Model 5 (close model)

Figure 7. RSO Shape Hypothesis Scenario II

Table 2. RSO Geometry for Proposed Models

RSO	Surface Area of Model
Model 1	80 80 60 60 60 60 m^2
Model 2	20 20 50 50 50 50 m^2
Model 3	30 30 100 50 100 50 m^2
Model 4	0.5 0.5 80 0.5 80 0.5 m^2
Model 5	80 80 50 50 50 50 m^2
Actual Model	80 80 60 50 60 50 m^2

weighted equally at the beginning of the MMAE process. The calculated probabilities over time from the MMAE algorithm are shown in Figure 8 for the second scenario. In this case it takes approximately the same time for all other models besides models one and five to converge to zero as in the first example. In this case models one and five fluctuate for the rest of the simulation time. This shows that the estimated object's shape is a function of both model one and five, which are both close to the true model.

The estimation errors, along with their respective 3σ bounds calculated from the covariance of the UKF, for attitude, position, velocity and rotation rate are shown in Figures 9. The attitude is estimated to within 1° of uncertainty, and attitude rate is found to within 1 deg/hr. Position and velocity are estimated to within 200 km and 0.02 km/s, respectively. All states show proper filter convergence behavior in that the residual errors settle down and are bounded by their computed 3σ bounds.

VIII. Conclusion

In this paper a multiple-model adaptive estimation with light curve and angles data was presented, which was used to identify the most probable shape of the RSO along with its associated rotational and translational states. Multiple-model adaptive estimation runs a bank of parellel filters to provide the state and model estimates using likelihood information and the previous conditional probability density function.

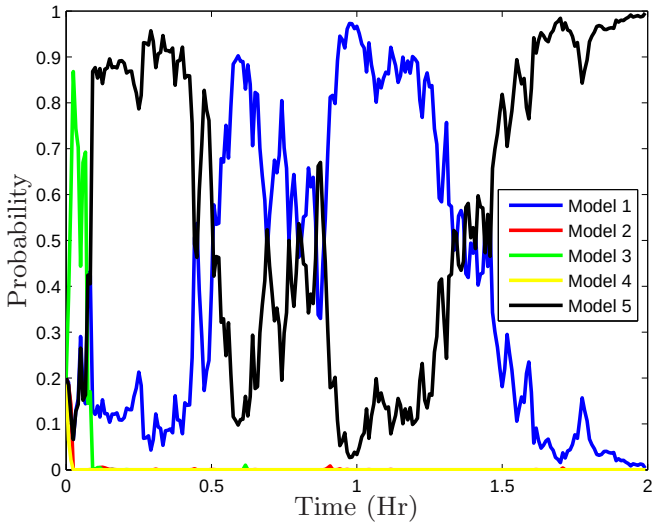

Figure 8. MMAE Consisting of Five RSO Models

The Unscented Kalman filter was used in the data reduction process. A solar radiation pressure model along with apparent brightness and angular location of the RSO are used to identify the shape of the object and its trajectory. Simulation results indicated that using a brightness magnitude model with solar radiation pressure effects is enough to estimate the proper shape geometry.

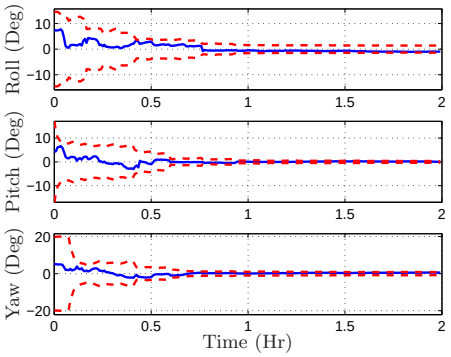

(a) Attitude Estimation Error

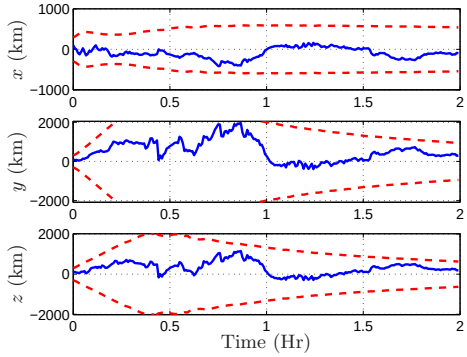

(b) Position Estimation Error

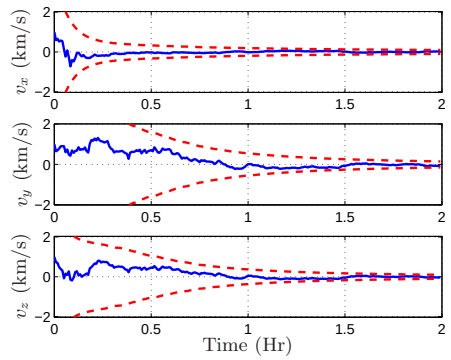

(c) Velocity Estimation Error

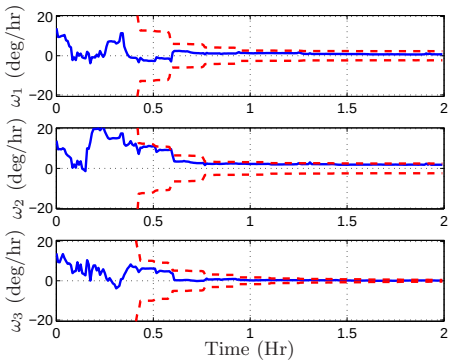

(d) Angular Velocity Estimation Error

Figure 9. RSO State Estimation Results

IX. Acknowledgement

This work was supported through multiple funding mechanisms, one of which was via the Air Force Research Laboratory, Space Vehicles Directorate (ASTRIA and Space Scholars program). The authors wish to thank Frank J. Centinello III for his work with Dr. Jah to further the research in light curve and angles data fusion.

References

[1]Sato, T., Wakayama, T., Tanaka, T., Ikeda, K.-i., and Kimura, I., "Shape of Space Debris as Estimated from Radar Cross Section Variations," *Journal of Spacecraft and Rockets*, Vol. 31, No. 4, Oct. 1994, pp. 665–670.

[2]Walker, J. L., "Range-Doppler Imaging of Rotating Objects," *IEEE Transactions on Aerospace and Electronics Systems*, Vol. AES-16, No. 4, Jan. 1980, pp. 23–52.

[3]Hagfors, T., "Mapping Planetary Surfaces by Radar," *Proceedings of the IEEE*, Vol. 61, No. 9, Jan. 1973, pp. 1219.

[4]DiMatteo, J., Florakis, D., Weichbrod, A., and Milam, M., "Proximity Operations Testing with a Rotating and Translating Resident Space Object," *AIAA Guidance, Navigation and Control Conference*, Aug. 2009, AIAA-2009-6293.

[5]Lichter, M. D. and Dubowsky, S., "State, Shape, and Parameter Estimation of Space Objects from Range Images," *Proceedings of Robotics: Science and Systems*, June 2005.

[6]Young, G.-S. J. and Chellappa, R., "3-D Motion Estimation using a Sequence of Noisy Stereo Images: Models, Estimation, and Uniqueness Results," *IEEE Transactions on Pattern Analysis and Machine Intelligance*, Vol. 12, No. 8, 1990, pp. 735–759.

[7]Broida, T. J. and Chellappa, R., "Estimating the Kinematics and Structure of a Rigid Object from a Sequence of Monocular Images," *IEEE Transactions on Pattern Analysis and Machine Intelligence*, Vol. 13, No. 6, 1991, pp. 497–513.

[8]Hall, D. T., Africano, J. L., Lambert, J. V., and Kervin, P. W., "Time-Resolved I-Band Photometry of Calibration Spheres and NaK Droplets," *Journal of Spacecraft and Rockets*, Vol. 44, No. 4, July 2007, pp. 910–919.

[9]Kaasalainen, M. and Torppa, J., "Optimization Methods for Asteriod Lightcurve Inversion I: Shape Determination," *Icarus*, Vol. 153, No. 4, Jan. 2001, pp. 24–36.

[10]Kaasalainen, M. and Torppa, J., "Optimization Methods for Asteriod Lightcurve Inversion II: The Complete Inverse Problem," *Icarus*, Vol. 153, No. 4, Jan. 2001, pp. 37–51.

[11]Calef, B., Africano, J., Birge, B., Hall, D., and Kervin, P., "Photometric Signature Inversion," *Proceedings of the International Society for Optical Engineering*, Vol. 6307, Aug. 2006, Paper 11.

[12]Jah, M. and Madler, R., "Satellite Characterization: Angles and Light Curve Data Fusion for Spacecraft State and Parameter Estimation," *Proceedings of the Advanced Maui Optical and Space Surveillance Technologies Conference*, Vol. 49, Wailea, Maui, HI, Sept. 2007, Paper E49.

[13]Centinello, F. J., "Six Degree of Freedom Estimation with Light Curve Data," Tech. rep., AFRL, Kihei, HI, 2008.

[14]Jazwinski, A. H., *Stochastic Processes and Filtering Theory*, chap. 8, Academic Press, San Diego, CA, 1970.

[15]Julier, S. J., Uhlmann, J. K., and Durrant-Whyte, H. F., "A New Approach for Filtering Nonlinear Systems," *Proceedings of the American Control Conference*, Seattle, WA, June 1995, pp. 1628–1632.

[16]Gordon, N. J., Salmond, D. J., and Smith, A. F. M., "Novel Approach to Nonlinear/Non-Gaussian Bayesian State Estimation," *IEE Proceedings, Part F - Communications, Radar and Signal Processing*, Vol. 140, No. 2, Seattle, WA, April 1993, pp. 107–113.

[17]Wetterer, C. J. and Jah, M., "Attitude Estimation from Light Curves," *Journal of Guidance, Control and Dynamics*, Vol. 32, No. 5, Sept.-Oct. 2009, pp. 16482.

[18]Shuster, M. D., "A Survey of Attitude Representations," *Journal of the Astronautical Sciences*, Vol. 41, No. 4, Oct.-Dec. 1993, pp. 439–517.

[19]Borderies, N. and Longaretti, P., "A New Treatment of the Albedo Radiation Pressure in the Case of a Uniform Albedo and of a Spherical Satellite," *Celestial Mechanics and Dynamical Astronomy*, Vol. 49, No. 1, March 1990, pp. 69–98.

[20]Ashikmin, M. and Shirley, P., "An Anisotropic Phong Light Reflection Model," Tech. Rep. UUCS-00-014, University of Utah, Salt Lake City, UT, 2000.

[21]Crassidis, J. L. and Markley, F. L., "Unscented Filtering for Spacecraft Attitude Estimation," *Journal of Guidance, Control and Dynamics*, Vol. 26, No. 4, July-Aug. 2003, pp. 536–542.

[22]Shuster, M. D., "A Survey of Attitude Representations," *Journal of the Astronautical Sciences*, Vol. 41, No. 4, Oct.-Dec. 1993, pp. 439–517.

[23]Schaub, H. and Junkins, J. L., "Stereographic Orientation Parameters for Attitude Dynamics: A Generalization of the Rodrigues Parameters," *Journal of the Astronautical Sciences*, Vol. 44, No. 1, Jan.-March 1996, pp. 1–20.

[24]Brown, R. G. and Hwang, P. Y. C., *Introduction to Random Signals and Applied Kalman Filtering*, John Wiley & Sons, New York, NY, 3rd ed., 1997, pp. 353–361.

[25]Stengel, R. F., *Optimal Control and Estimation*, Dover Publications, New York, NY, 1994, pp. 402–407.

[26]Anderson, B. D. O. and Moore, J. B., *Optimal Filtering*, chap. 10.1, Dover Publications, Mineola, NY, 2005.

[27]Anderson, B. D. O., Moore, J. B., and Hawkes, R. M., "Model Approximations via Prediction Error Identification," *Automatica*, Vol. 14, No. 6, Nov. 1978, pp. 615–622.